Low-temperature admittance spectroscopy for defect characterization in Cu(In,Ga)(S,Se)$_2$ thin-film solar cells

Jonathan Parion,
Romain Scaffidi
and
Denis Flandre
ICTEAM (UCLouvain)
Louvain-la-Neuve, Belgium
Contact: jonathan.parion@hotmail.be

Guy Brammertz[1,2,3]
and
Bart Vermang[1,2,3]
[1]*imec division IMOMEC (partner in Solliance)*
[2]*Institute for material research (IMO)*
[3]EnergyVille 2, Thorpark 8320,
Genk, Belgium

IEEE EUROCON 2023 - 20th International Conference on Smart Technologies | 978-1-6654-6397-3/23/$31.00 ©2023 IEEE | DOI: 10.1109/EUROCON56442.2023.10199008

***Abstract*—We present a methodology to use low-temperature admittance measurements for characterizing defects in thin-film Cu(In,Ga)(S,Se)$_2$ solar cells, which is a major step towards increased performance. We develop the theory behind admittance spectroscopy at both room and low temperature, focusing on the so-called "loss-map" graphical representation. It allows to distinguish the entangled responses of different loss mechanisms and, combined with SCAPS 1-D simulations, leads to a refined interpretation of experimental admittance measurements. Using this methodology on experimental measurements, we identify the likely presence of an interface defect, and extract its activation energy ($\mathbf{E_A = 0.093\,eV}$) and capture cross-section ($\sigma = \mathbf{2.88 \cdot 10^{-18}\,cm^2}$).**

***Index Terms*—Admittance spectroscopy, CIGS, thin-film PV**

I. Introduction

In the context of photovoltaic (PV) solar energy, thin-film Cu(In,Ga)(S,Se)$_2$ (CIGS) solar cells (Fig. 1) have emerged as a promising technology, mainly due to the good absorption properties of CIGS and to the cells' reduced thickness that lowers raw material needs and enhances urban integration [1]. For this technology to reach its full potential, some challenges need to be tackled. The most complex is the high density of defects that constitutes a major limitation to performance [2]. To overcome this, a deeper understanding of the defects nature is required, namely their location (bulk or interface), their activation energy E_A and their capture cross section σ. This can be attained with one particularly powerful method for characterizing defects called admittance spectroscopy (AS) [3]–[15]. Indeed, measuring the admittance at different voltages, frequencies and temperature enable to observe the charge response of defects and finally extract important properties such as E_A and σ. In this work, we use an innovative graphical representation for room temperature AS [3] and we extend its use to low-temperature AS. First, the AS theory is applied to the study of defects using a simple simulation model. Second, the "loss map" analysis tool is presented as a solution to distinguish the signature of not only defects but also other loss mechanisms. Finally, the developed methodology allows a deeper interpretation of admittance measurements obtained on an actual CIGS solar cell.

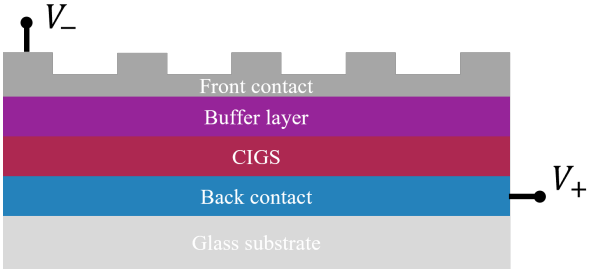

Fig. 1: Schematic representation of a CIGS solar cell

II. Theory

A. Admittance spectroscopy

The admittance $Y(\omega)$ can be represented by the parallel connection of a capacitance and a conductance, that both depend on the measurement frequency [4]. It is expressed as:

$$Y(\omega) = G(\omega) + j\omega C(\omega). \tag{1}$$

The two parts of this admittance, the conductance $G(\omega)$ and the capacitance $C(\omega)$, are linked to each other through the Kramers-Kronig relations. These prove mathematically that the analysis of the two quantities is equivalent [5]. In this work and in the literature [3]–[11], the focus is typically put on capacitance measurements because they are less affected by parasitic conductive elements and can thus be more accurately measured.

In solar cells, the capacitance is mainly related to the depletion region of the PN junction. For an ideal PN junction, the depletion capacitance is [16]:

$$C_d = \frac{\varepsilon_s}{w_d}, \tag{2}$$

with ε_s the material dielectric constant and w_d the depletion length. Since w_d is independent from the measurement frequency, the same is true for C_d.

Because CIGS solar cells are essentially non-ideal PN junctions, other capacitive contributions such as bulk defects, interface defects, series resistance and interface barriers are added to C_d to form the total capacitance C_{tot}. All of these contributions have a so-called characteristic frequency f_c beyond which they stop contributing to C_{tot}.

Suppose an acceptor bulk defect in the CIGS layer, the energy level of which is crossed by the quasi-Fermi level for holes. If an AC voltage is applied, some of the defect states are successively charged and discharged as the Fermi level is moving across it. A condition for this to happen is that the frequency of the signal is not higher than the charge capture and emission rates. Above its characteristic frequency, this is not the case anymore and the defect therefore stops contributing to C_{tot}. This is shown in the simulation from Fig. 2, where a bulk defect is added to an ideal CIGS solar cell. As expected, C_{tot} is high at low frequency due to the contribution of the bulk defect, and decreases for frequencies higher than f_c.

The characteristic frequency of the defect is derived from the time constant of the charge emission process, and is given by [16]:

$$f_c = \frac{1}{2\pi}\,\sigma\, v_T\, N_v\, \exp\left(\frac{-E_A}{kT}\right), \tag{3}$$

with σ the capture cross section of the defect, v_T the thermal velocity of holes, N_v the density of states in the valence band, E_A the activation energy of the defect and kT the thermal energy.

It is clear from Fig. 2 that voltage bias also influences the action of the defect on the total capacitance. From the PN junction theory, it is known that the distance between the quasi-Fermi level for holes and electrons is changed by the voltage bias. The effect of different voltage biases on the solar cell bandstructure is represented in Fig. 3. Following

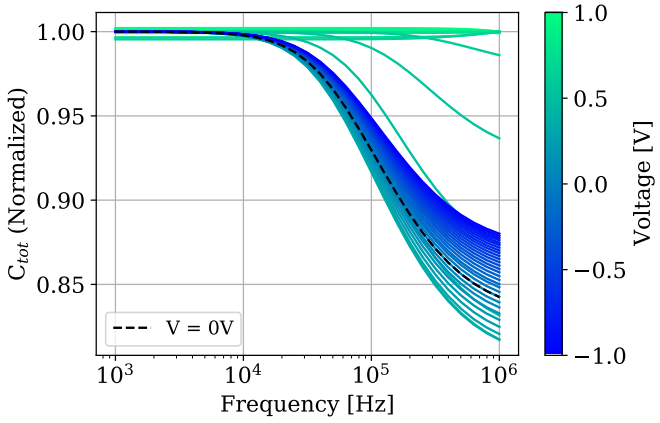

Fig. 2: SCAPS [17] simulation of the normalized total capacitance versus frequency and voltage, for a CIGS solar cell with an added acceptor bulk defect with parameters $E_A = 0.326\,\text{eV}$, $\sigma = 10^{-15}\,\text{cm}^2$ and $N_t = 10^{16}\,\text{cm}^{-3}$

the Fermi-Dirac statistic, an acceptor state is occupied when the quasi-Fermi level for holes F_p is placed below it. In the context of defects, this means that an acceptor defect such as the one considered here is fully ionized when its state is above F_p. The same is valid for a donor defect placed below the quasi-Fermi level for electrons F_n. Following the Pauli exclusion principle, a defect state is only able to participate to the charge capture/release process when it is not fully ionized.

This explains the trend visible in Fig. 2, where the defect contribution to capacitance changes with respect to voltage bias. When the defect level is entirely above F_p, such as when $V = 1\,\text{V}$ (Fig. 3(c)), the defect is not able to exchange charges and hence does not contribute to the total capacitance. On the contrary, when F_p crosses the level of the defect, part of the defect states are ionized and it contributes to the total capacitance (Fig. 3(a) and 3(b)). In this case, because the defect is a bulk defect present over the entire CIGS thickness, the voltage range in which the defect is active is large. The active defect states are not the same at $V = -1\,\text{V}$ (Fig. 3(a)) and at $V = 0\,\text{V}$ (Fig. 3(b)).

Another way of representing the defect response is to take the opposite of capacitance derivative with respect to frequency, multiplied by the frequency ($-fdC/df$). This is shown in Fig. 4(a). The first information that is extracted from this figure is the characteristic frequency. Indeed, it is around that frequency that the change in capacitance is the biggest, which is materialized by a peak in the $-fdC/df$ curve. In this case, $f_c = 100\,\text{kHz}$. Looking at the voltage dependency, it appears that the derivative capacitance increases with voltage bias, before reaching a maximum around 0.5 V and then decreasing rapidly close to 1 V. The increase in derivative capacitance from -1 V to 0.5 V is coming from the increase in depletion capacitance that is modulating the $-fdC/df$ characteristic. At -1 V, the width of the depletion region is greater and C_d is lower. With bias voltage increasing,C_d and C_{tot} increase and so does their derivative. Beyond 0.5 V, the characteristic is physically explained by the position of F_p which stays below the defect level. In that condition, all of the defect states are fully ionized and do not contribute to the capacitance anymore, hence the derivative capacitance rapidly falls to zero.

Although this representation gives a full overview of the defect capacitive behaviour and enables the extraction of its characteristic frequency, interpreting all the superimposed $-fdC/df$ curves at different voltages is far from easy. This is even more true when multiple loss mechanisms affect the studied structure simultaneously. For this reason, another representation called the "CVf loss map", first proposed in [3] and shown in Fig. 4(b), is preferred. In the SCAPS simulations where loss maps are used, the voltage is swept up to 0.75 V and not 1 V such as in experimental measurements. This is because the junction capacitance is more significant compared to the depletion capacitance after 0.75 V, which makes it difficult to interpret the simulations with the AS methodology. This is not an issue since the operating range of solar cells is below V_{oc} whose value is rarely greater that $0.7 - 0.8\,\text{V}$ for CIGS solar

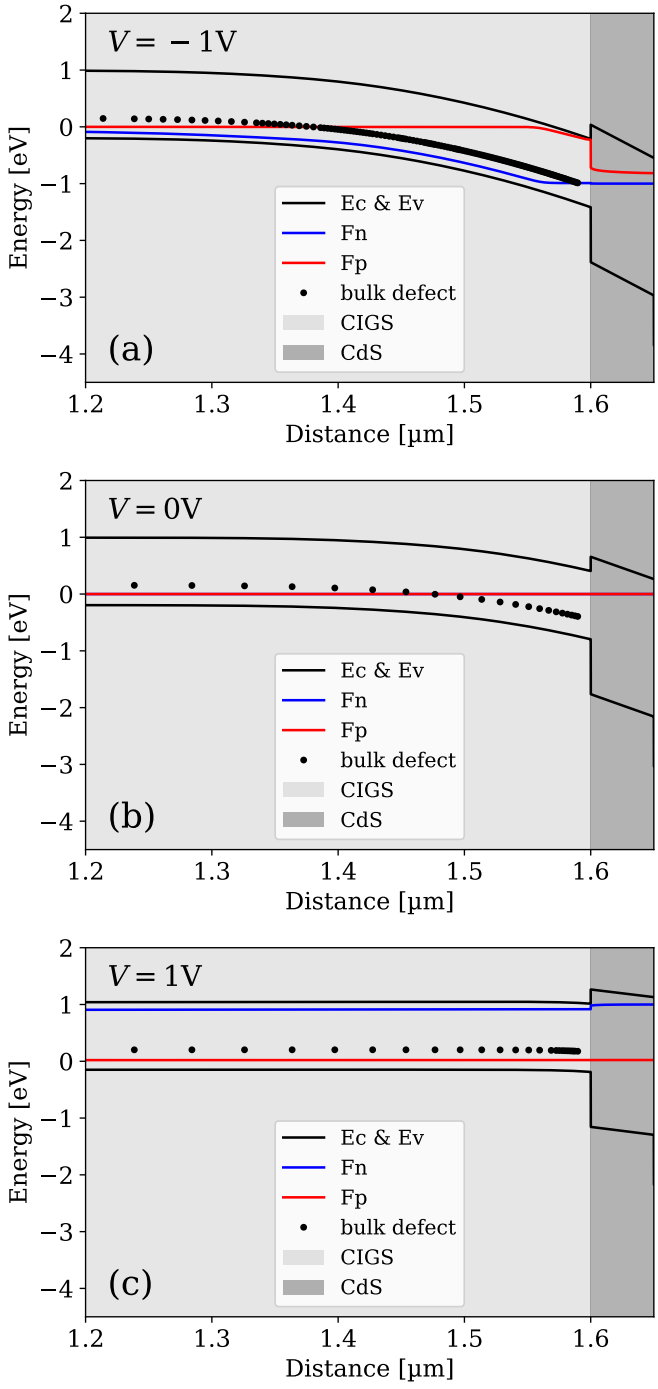

Fig. 3: SCAPS simulation of the band structure for a CIGS solar with the same acceptor bulk defect as in Fig. 2, at bias voltages of (a) $V = -1\,\mathrm{V}$, (b) $V = 0\,\mathrm{V}$, (c) $V = 1\,\mathrm{V}$. Because the introduced defect is an acceptor, the position of the Fermi level for holes has to be considered for evaluating the charge state of the defect.

cells. Here, the bulk defect presents a broad signature along the voltage range, coming from the fact that the Fermi level is crossing the defect level at many different biases (Fig. 3). In the frequency range, it is concentrated around the 100kHz response frequency that characterizes the defect.

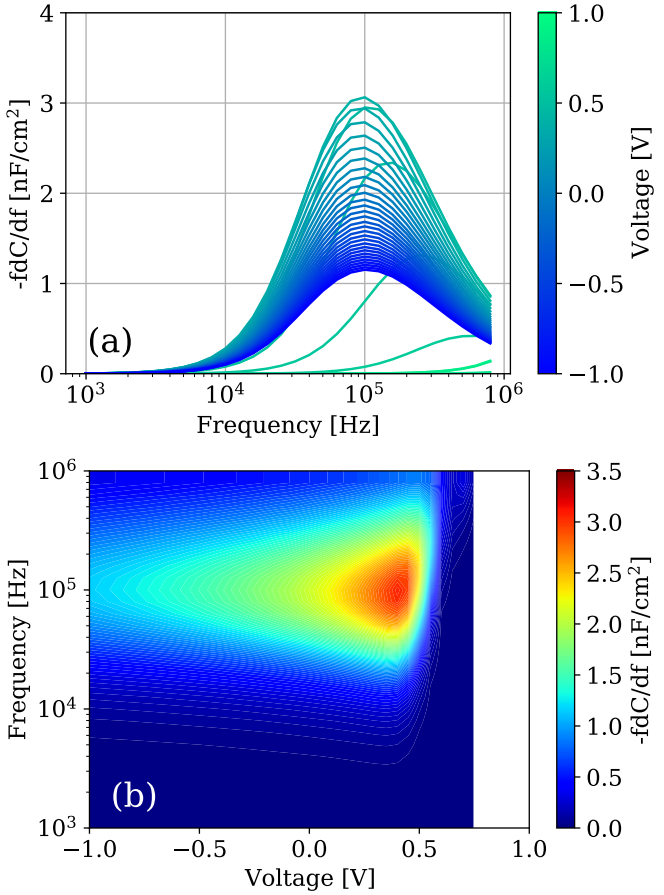

Fig. 4: SCAPS simulation of $-fdC/df$ characteristic for a CIGS solar with the same acceptor bulk defect as in Fig. 2 and using (a) the traditional representation and (b) the novel CVf loss map representation.

SCAPS can be used in complement to the loss map representation to identify defects signatures, but also other types of losses such as interface barriers or series resistances. In Fig. 5, the response of an interface defect, and the coupled response of a bulk defect and a series resistance are represented. Interface defects (Fig. 5(a)) present a much more localized signature on the map than bulk defects. This comes from the defect level being very localized in the bandgap and the Fermi level therefore crossing it at a very particular bias point. The width of the response is generally a practical way of distinguishing these two types of defects. In the same way as for bulk defects, the peak in capacitance derivative for interface defects is also localized around its characteristic energy.

When performing simulations of AS measurements, it is of particular interest to consider several losses at the same time (Fig. 5(b)). This is often encountered in experimental solar cells, where a series resistance can, for example, be combined with a bulk defect. In the presence of multiple losses, it appears that the different traces simply add up on the map [3], [4]. In function of the voltage and frequency content of these losses, the map can quickly become complex to interpret. This is a

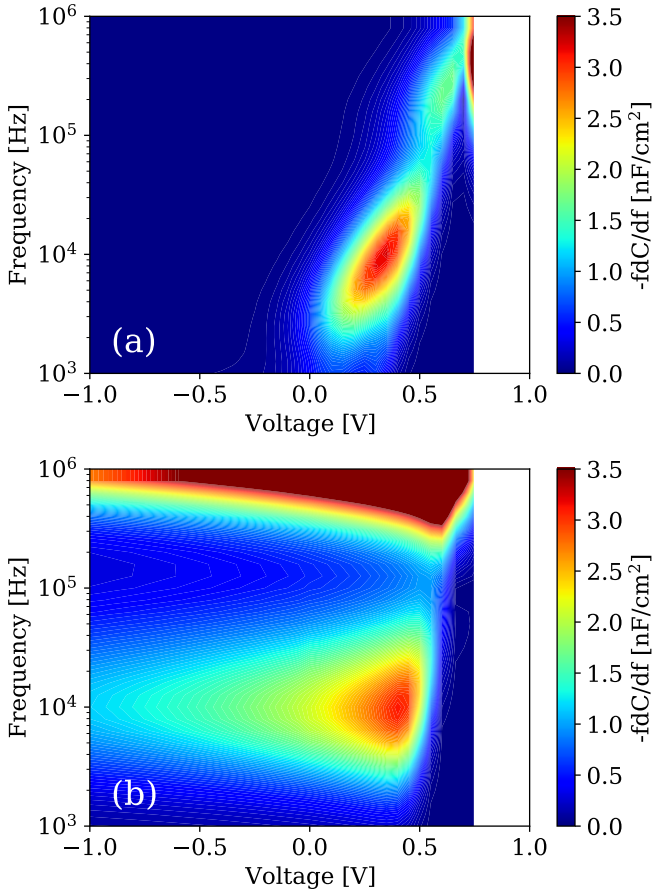

Fig. 5: SCAPS loss maps for (a) a donor interface defect and (b) a bulk defect combined with a series resistance.

limitation of this representation that was already previously mentioned [3], and is a key motivation to use low-temperature measurements for decoupling losses.

B. Low-temperature admittance spectroscopy

In (3), it is highlighted that the characteristic frequency of defects depends on two main parameters: σ and E_A. As shown in this equation, using one fixed temperature and with v_{th} and N known, it is impossible to extract these two parameters independently from each other. Fortunately, by introducing another degree of freedom in the measurement, i.e. the measurements temperature, it is possible to decouple these two quantities and to extract their value.

The kinetics of a thermally activated process is commonly described by the Arrhenius equation [18]:

$$r = r_0 \exp\left(\frac{-E_A}{RT}\right), \tag{4}$$

where r is the kinetic reaction rate, r_0 is the pre-exponential factor, E_A is the activation energy, R is a thermodynamic constant and T is the absolute temperature. In the case of the charge emission rate e_c from a certain energy level, here the defect level, the equation is rewritten as [19]:

$$e_c = 2\pi f_c = \xi_0 T^2 \exp\left(\frac{-E_A}{kT}\right), \tag{5}$$

with f_c the defect characteristic frequency as defined before, and $\xi_0 T^2$ the pre-exponential factor. This is directly related to equation (3). By association, and by considering the temperature dependency of both v_T and N, it is possible to obtain the following Arrhenius equation:

$$\frac{\omega_t}{T^2} = \sigma\, v_{T,0}\, N_0 \exp\left(\frac{-E_A}{kT}\right). \tag{6}$$

By using admittance measurements versus bias and frequency, different characteristic frequencies can be extracted for each measurement temperature. These points are then plotted on the so-called Arrhenius plot. Finally, when fitting the data obtained at each temperature with a linear model, σ and E_A can be extracted.

III. Experimental validation

In this section, the theory developed before is applied to the characterization of an experimental CIGS solar cell. Admittance measurement are conducted using an *Agilent E4980A* LCR meter. The voltage bias is varied between -1 V and 1 V, with an AC amplitude of 50 mV, and the frequency is swept from 1 kHz to 1 MHz. Low-temperature measurements are performed in open air, between 133 K and 268 K and by steps of 20 K. The highest temperature is taken just below the freezing point of water.

The CVf loss map of the experimental cell, realized at room temperature, is presented in Fig. 6. This map presents a broad signature at high frequencies, that reduces slightly in frequency at high voltage bias. From the main capacitively active loss mechanisms presented before, the most likely to present such a signature is the device series resistance R_s. Indeed, when R_s is sufficiently high in a device, it induces a reduction in the measured capacitance C_m at high frequency [20]:

$$C_m(j\omega) = C_d \cdot \begin{cases} 1, & \text{if } \omega \text{ is small} \\ 1/(\omega R_s C_d)^2, & \text{if } \omega \text{ is large} \end{cases} \tag{7}$$

with ω the measurement angular frequency. The effect induced by R_s is typically active at frequencies close to 1MHz, which is the case here. In Eq. (7) it also appears that C_m is bias

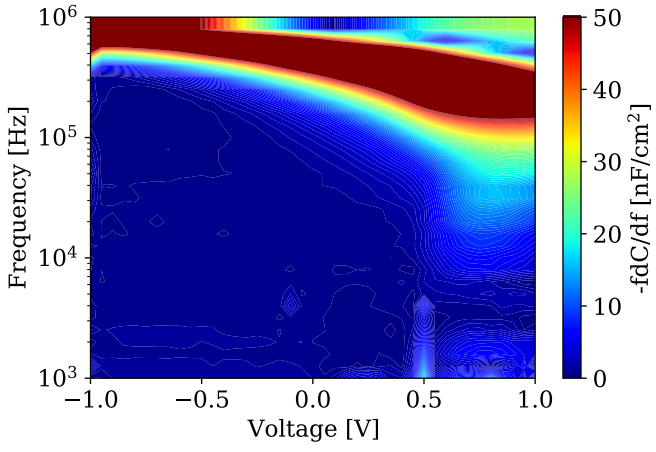

Fig. 6: Admittance measurement of an experimental CIGS solar cell, using the loss map representation presented before.

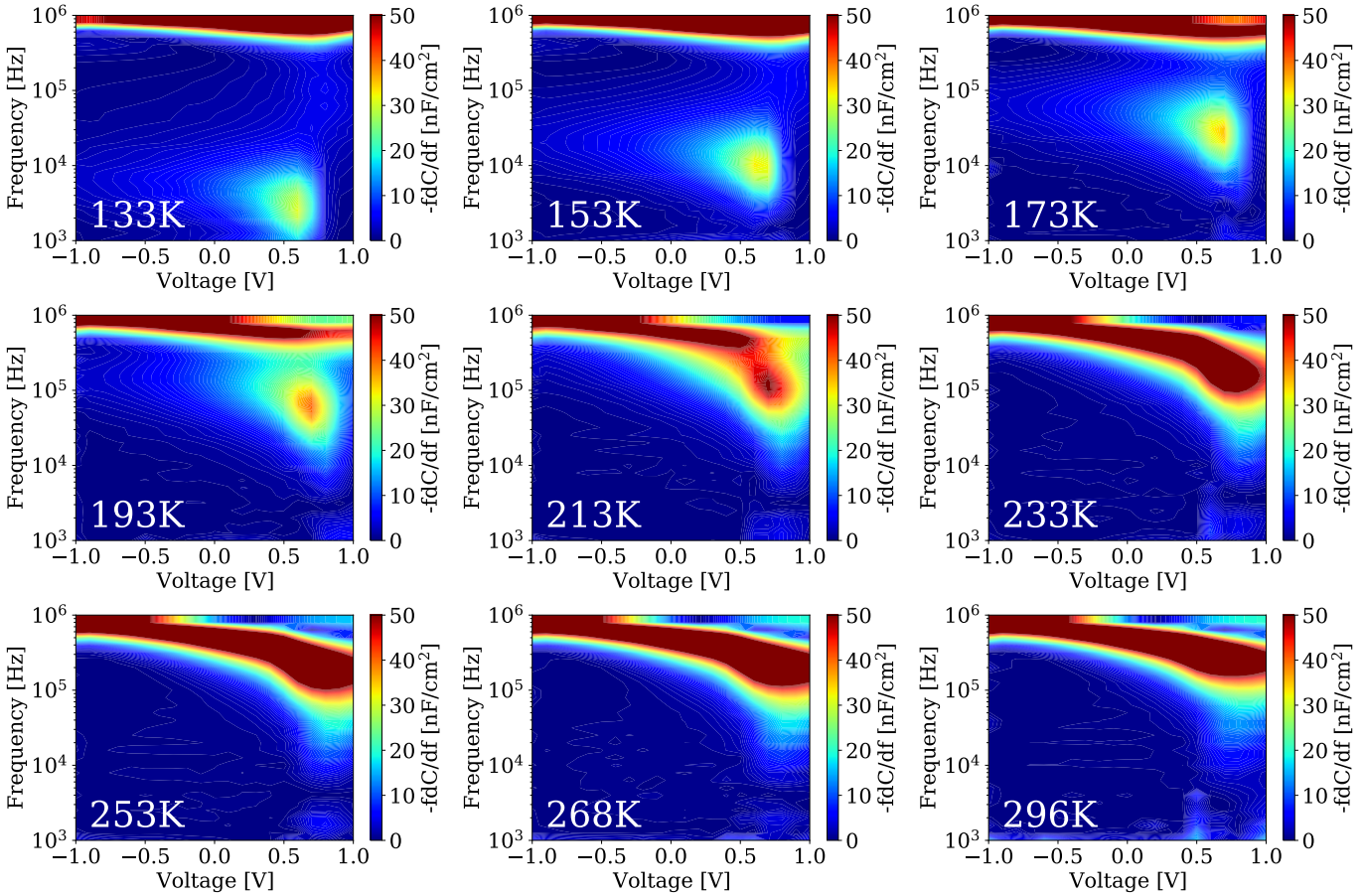

Fig. 7: Admittance measurements at different temperature bias of an experimental CIGS solar cell, using the loss map representation presented before. Two signatures are visible on the different maps. The wide signature appearing on the top of the map, that is mostly independent from temperature variation, is likely coming from the effect of a series resistance. The narrow signature that is moving with respect to temperature variation is likely a defect.

independent, as this is the case for C_d and R_s. This is only true under the assumption that the total capacitance is composed of C_d only. In the present case, it appears that there is a slight decrease in frequency for higher voltage biases. This could be caused by the action of another loss mechanism, such as a bulk or interface defect. The defect does have a bias dependant action and contributes to C_m hence resulting in the trace from Fig. 6.

By considering solely the room temperature admittance measurement, it is not possible to confirm or deny this hypothesis. This is a great motivation for performing low-temperature AS, as it is known from the theory that defect-like mechanisms see their characteristic frequency change with temperature. The CVf loss maps realized from AS measurements at several temperatures are presented in Fig. 7. These measurements confirm the presence of another capacitive loss than R_s, likely an interface defect. Indeed, it seems to be concentrated around a certain value of voltage, which is the one at which the Fermi level would be crossing the interface level of the defect. It is very unlikely that this signature is the one of a bulk defect, because it would be much wider in the voltage range as shown in Fig. 4(b) and as discussed in [3]. Its characteristic frequency increases with the temperature increasing, and merges above 213 K with the response of R_s, which explains the observations made previously.

By extracting the characteristic frequency of the defect at several temperature bias points, it is possible to obtain the Arrhenius plot of Fig. 8.

When fitting the data with a linear interpolation, it is then possible to extract the activation energy and capture cross section of the defect as follow:

$$\begin{cases} \sigma = \dfrac{e^b}{v_{T,0}\, N_0} = 2.88 \cdot 10^{-18}\,\mathrm{cm}^2 \\ E_A = -a \cdot 1000k = 93\,\mathrm{meV} \end{cases} \tag{8}$$

This defect is considered to be shallow [3], with a rather low σ. This means that it should not impact much the performance of the device contrarily to the high R_s visible in this cell.

IV. Conclusion

In this work, the theory behind admittance spectroscopy at room and low temperature is developed. The so-called loss map is presented as a visual representation of admittance measurements. When coupling AS with SCAPS simulations, it was possible to identify clearly the response of several loss mechanisms inside a CIGS solar cell, such as bulk and interface

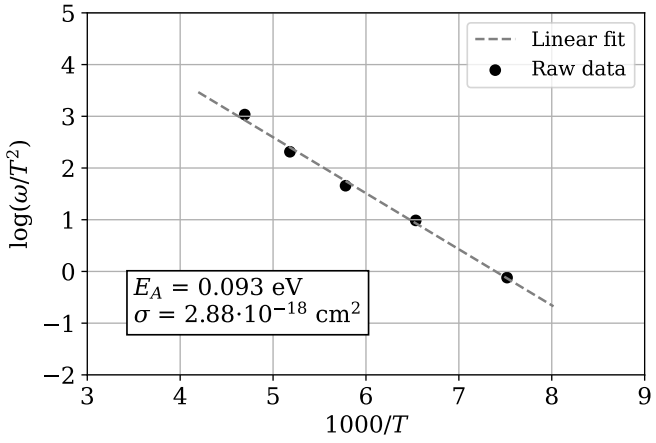

Fig. 8: Arrhenius plot made with the data from Fig. 7. Each point is obtained by extracting the characteristic frequency of the defect at one particular bias point. For higher temperatures ($T \geq 233$ K), the data was not exploited due to the high correlation of the series resistance and defect signatures.

defects but also series resistances. It was shown experimentally that room-temperature measurements are sometimes not sufficient to fully characterize the cell, and low-temperature loss maps were therefore introduced as a way of decoupling several losses. It was possible to discover an interface defect, with $E_A = 0.093$ eV and $\sigma = 2.88 \cdot 10^{-18}$ cm^2, whose action was coupled to the one of R_s at room temperature. In the end, it appears that room- and low-temperature AS constitutes a robust method for the advanced characterization of CIGS solar cells and should be key in the future improvement of this technology.

ACKNOWLEDGMENT

This project has received funding from the European Union's Horizon 2020 research and innovation programme under grant agreement No 850937. The author would like to thank Avancis for providing the absorber in the experimental cell.

REFERENCES

[1] T. D. Lee and A. U. Ebong, 'A review of thin film solar cell technologies and challenges', Renewable and Sustainable Energy Reviews, vol. 70, pp. 1286–1297, Apr. 2017, doi: 10.1016/j.rser.2016.12.028.

[2] M. Ochoa, S. Buecheler, A. N. Tiwari, and R. Carron, 'Challenges and opportunities for an efficiency boost of next generation Cu(In,Ga)Se2 solar cells: prospects for a paradigm shift', Energy and Environmental Science, vol. 13, no. 7, pp. 2047–2055, 2020, doi: 10.1039/d0ee00834f.

[3] G. Brammertz et al., 'Bias-Dependent Admittance Spectroscopy of Thin-Film Solar Cells: Experiment and Simulation', IEEE Journal of Photovoltaics, vol. 10, no. 4, pp. 1102–1111, 2020, doi: 10.1109/JPHOTOV.2020.2992350.

[4] Decock, Koen, 'Defect related phenomena in chalcopyrite based solar cells', PhD Thesis, Ghent University, Department of Electronics and information systems, 2012.

[5] C. León, J. M. Martin, J. Santamaría, J. Skarp, G. González-Díaz, and F. Sánchez-Quesada, 'Use of Kramers–Kronig transforms for the treatment of admittance spectroscopy data of p-n junctions containing traps', Journal of Applied Physics, vol. 79, no. 10, pp. 7830–7836, 1996, doi: 10.1063/1.362391.

[6] J. Kneisel, K. Siemer, I. Luck, and D. Bräunig, 'Admittance spectroscopy of efficient CuInS2 thin film solar cells', Journal of Applied Physics, vol. 88, no. 9, pp. 5474–5481, Nov. 2000, doi: 10.1063/1.1312838.

[7] T. Eisenbarth, T. Unold, R. Caballero, C. A. Kaufmann, and H.-W. Schock, 'Interpretation of admittance, capacitance-voltage, and current-voltage signatures in Cu(In,Ga)Se2 thin film solar cells', Journal of Applied Physics, vol. 107, no. 3, p. 034509, Feb. 2010, doi: 10.1063/1.3277043.

[8] J. Heath and P. Zabierowski, 'Capacitance Spectroscopy of Thin-Film Solar Cells', in Advanced Characterization Techniques for Thin Film Solar Cells, 1st ed., D. Abou-Ras, T. Kirchartz, and U. Rau, Eds. Wiley, 2011, pp. 81–105. doi: 10.1002/9783527636280.ch4.

[9] R. Herberholz, M. Igalson, and H. W. Schock, 'Distinction between bulk and interface states in CuInSe2/CdS/ZnO by space charge spectroscopy', Journal of Applied Physics, vol. 83, no. 1, pp. 318–325, Jan. 1998, doi: 10.1063/1.366686.

[10] P. Krispin, 'Single-level interface states in semiconductor structures investigated by admittance spectroscopy', Appl. Phys. Lett., vol. 70, no. 11, Art. no. 11, Mar. 1997, doi: 10.1063/1.118598.

[11] T. Walter, R. Herberholz, C. Müller, and H. W. Schock, 'Determination of defect distributions from admittance measurements and application to Cu(In,Ga)Se2 based heterojunctions', Journal of Applied Physics, vol. 80, no. 8, pp. 4411–4420, Oct. 1996, doi: 10.1063/1.363401.

[12] D. Abou-Ras, T. Kirchartz, and U. Rau, Eds., Advanced Characterization Techniques For Thin Film Solar Cells. Weinheim, Germany: Wiley, 2016.

[13] J. V. Li, S. W. Johnston, Y. Yan, and D. H. Levi, 'Measuring temperature-dependent activation energy in thermally activated processes: A 2D Arrhenius plot method', Rev. Sci. Instrum., 2010.

[14] J. V. Li and D. H. Levi, 'Determining the defect density of states by temperature derivative admittance spectroscopy', Journal of Applied Physics, vol. 109, no. 8, Art. no. 8, Apr. 2011, doi: 10.1063/1.3573538.

[15] F. H. Seymour, V. Kaydanov, and T. R. Ohno, 'Simulated admittance spectroscopy measurements of high concentration deep level defects in CdTe thin-film solar cells', J. Appl. Phys., 2006.

[16] J.-P. Colinge and C. A. Colinge, Physics of Semiconductor Devices. Kluwer Academic Publishers, 2002.

[17] M. Burgelman and others, 'SCAPS: a Solar Cell Capacitance Simulator', Feb. 2021.

[18] S. A. Ashter, 'Mechanics of Materials', in Thermoforming of Single and Multilayer Laminates, Elsevier, 2014, pp. 123–145. doi: 10.1016/b978-1-4557-3172-5.00006-2.

[19] A. Krysztopa, M. Igalson, Y. Aida, J. K. Larsen, L. Gütay, and S. Siebentritt, 'Defect levels in the epitaxial and polycrystalline CuGaSe2 by photocurrent and capacitance methods', Journal of Applied Physics, vol. 110, no. 10, p. 103711, Nov. 2011, doi: 10.1063/1.3662198.

[20] J. H. Scofield, 'Effects of series resistance and inductance on solar cell admittance measurements', Solar Energy Materials and Solar Cells, vol. 37, no. 2, pp. 217–233, May 1995, doi: 10.1016/0927-0248(95)00016-x.